

## Research Article

# Effect of Process Parameters on Short Fiber Orientation along the Melt Flow Direction in Water-Assisted Injection Molded Part

Haiying Zhou <sup>1,2</sup>, Hesheng Liu <sup>1,2</sup>, Qingsong Jiang,<sup>2</sup> Tangqing Kuang,<sup>3</sup> Zhixin Chen,<sup>2</sup> and Weiping Li<sup>2</sup>

<sup>1</sup>School of Mechanical and Electrical Engineering, Nanchang University, Nanchang 330031, China

<sup>2</sup>Jiangxi Province Key Laboratory of Polymer Micro/Nano Manufacturing and Devices, East China University of Technology, Nanchang 330013, China

<sup>3</sup>School of Mechanical and Electrical Engineering, East China Jiaotong University, Nanchang 330013, China

Correspondence should be addressed to Hesheng Liu; [hsliu@vip.163.com](mailto:hsliu@vip.163.com)

Received 21 February 2019; Revised 8 July 2019; Accepted 22 July 2019; Published 19 August 2019

Academic Editor: Francisco Chinesta

Copyright © 2019 Haiying Zhou et al. This is an open access article distributed under the Creative Commons Attribution License, which permits unrestricted use, distribution, and reproduction in any medium, provided the original work is properly cited.

The short fiber orientation (SFO) distribution in the water-assisted injection molding (WAIM) is more complicated than that in traditional injection molding due to the new process parameters. In this work, an improved fiber orientation tensor method was used to simulate the SFO in WAIM. The result was compared with the scanning electron micrograph, which was consistent with the experiments. The effect of six process parameters, including filling time, melt temperature, mold temperature, delay time, water pressure, and water temperature, on the SFO along the melt flow direction were studied through orthogonal experimental design, range analysis, and variance analysis. An artificial neural network was used to establish the nonlinear agent model between the process parameters and  $A_{11}$  representing the fiber orientation in melt flow direction. Results show that water pressure, melt temperature, and water temperature have significant effects on SFO. The three-dimensional (3D) response surfaces and contour plots show that the values of  $A_{11}$  decrease with the increase in water pressure and melt temperature and increase as the water temperature rises.

## 1. Introduction

With the development of advanced, economical, and environmentally friendly society, higher requirements are placed on the performance of plastic products. The short-fiber-reinforced polymer composite (SFRPC) is a material with a polymer as a matrix and short fibers as a dispersed phase. Its characteristics are lightweight, high specific strength and specific modulus, stable chemical properties, heat resistance, and good wear resistance [1]. In recent years, SFRPCs have gradually replaced metal materials in some fields, making them widely used in aviation, automotive, shipping, and medicine [2, 3].

Fluid-assisted injection molding is an emerging process that includes gas-assisted injection molding (GAIM) and water-assisted injection molding (WAIM) [4, 5]. The fluids used in GAIM and WAIM are nitrogen and water, respectively. Due to incompressibility, high heat capacity,

and good thermal conductivity of water, the advantages of WAIM over GAIM are high product efficiency, more uniform and thinner residual wall thickness (RWT) [6]. Based on whether or not the cavity is completely filled with melt, WAIM can be categorized into two types: short-shot WAIM and overflow WAIM. In short-shot WAIM, the mold cavity is partially filled with melt, followed by the injection of water into the core of melt. In overflow WAIM, the mold cavity is completely filled with melt, followed by the injection of water that pushes the melt into the overflow cavity to form a part with a hollow cross section. Compared with the standard injection molding, WAIM offers significant advantages in the preparation of shaped hollow plastic parts with uniform RWT. However, due to the difficulty in controlling the water injection pressure and the turbulence characteristics of the injection water, the quality of the products is not stable [7, 8]. Present researches on WAIM focus on the

distribution of RWT [9], the length of water column penetration [10, 11], and the defects of molded parts [12, 13].

The RWT of water-assisted injection molded parts is thin, and the mechanical properties of the parts can be greatly improved by using SFRPC as a raw material. Many studies reported that the distribution of short fiber orientation (SFO) determined the mechanical and physical properties of the plastic parts, while fiber orientation was affected by mold structure, molding process parameters, flow field distribution, initial state of fibers, fiber properties, and matrix properties [14–16]. The molding process parameters influence temperature, velocity distribution, melt viscosity gradient, and flow field, which ultimately determine the fiber orientation. Liu et al. [7, 12] found that the short fibers mostly aligned along the melt flow direction in WAIM. Huang et al. [17] suggested that high-pressure water penetration significantly affected fiber orientation in WAIM, and increasing melt temperature decreased fiber orientation. Systematic studies on the influence of process parameters on the SFO help understand the fiber orientation mechanism, optimize the SFO distribution, and improve the overall performance of the parts in WAIM.

WAIM, including the melt and high-pressure water filling stages, is more complicated than the standard injection molding process. Due to the difficulty in accurately controlling all the process parameters simultaneously, the research of SFO in laboratory is performed for qualitative analysis. With the development of computer technology, the three-dimensional numerical simulation technology developed rapidly, enabling simulating complex injection molding. The process parameters can be accurately controlled in simulation, but the reliability of SFO simulation depends on the accuracy of the mathematical model. The fiber orientation distribution in injection molding is very complicated microscopically. In the past three decades, theoretical studies on fibers suspension rheology have achieved a great success. Based on the classic fiber orientation models, including Jeffery hydrodynamics model, Folgar–Tucker model [18], and ARD-RSC model [19], Tseng et al. recently proposed an improved iARD-RPR model [20, 21], which can provide good simulation results of SFO in standard injection molding.

In this work, based on the iARD-RPR model, the SFO in WAIM was simulated, and the results were compared with the scanning electron micrographs (SEMs) to verify the applicability of this model for WAIM. The influences of process parameters on the fiber orientation along the melt flow direction were studied through the methods of orthogonal experimental design, range analysis, and variance analysis. The nonlinear proxy model between process parameters and fiber orientation along the melt flow direction was constructed by artificial neural network (ANN), and the interaction effect of significant process parameters was investigated using 3D response surfaces and contour plots.

## 2. Methods

**2.1. Fluid Mechanics Governing Equations.** The movement of short fibers in injection molding is a transient, non-

Newtonian, and nonisothermal process. In numerical simulations, the melt is considered to be incompressible and laminar, and the inertial term is ignored. The governing equations for transient and nonisothermal fluid motion in WAIM processes are as follows:

$$\begin{aligned} \frac{\partial \rho}{\partial t} + \nabla \cdot (\rho \mathbf{u}) &= 0, \\ \frac{\partial}{\partial t} (\rho \mathbf{u}) + \nabla \cdot (\rho \mathbf{u} \mathbf{u} - \boldsymbol{\sigma}) &= \rho \mathbf{g}, \\ \boldsymbol{\sigma} &= -p \mathbf{I} + \eta (\nabla \mathbf{u} + \nabla \mathbf{u}^T), \\ \rho C_p \left( \frac{\partial T}{\partial t} + \mathbf{u} \cdot \nabla T \right) &= \nabla \cdot (k \nabla T) + \eta \dot{\gamma}^2, \end{aligned} \quad (1)$$

where  $\mathbf{u}$  is the velocity vector,  $\eta$  is the shear viscosity,  $p$  is the pressure,  $\rho$  is the melt density,  $\boldsymbol{\sigma}$  is the total stress tensor,  $\mathbf{g}$  is the gravity,  $C_p$  is the specific heat capacity,  $T$  is the temperature,  $k$  is the thermal conductivity,  $t$  is the time, and  $\dot{\gamma}$  is the shear rate.

**2.2. Rheological Model.** The Cross-WLF rheological model with seven parameters was used in the simulation, which can describe complex viscosity behaviors, including the viscosity varying with shear rate and the zero-shear-rate viscosity, depending on temperature and pressure [20].

$$\begin{aligned} \eta(\dot{\gamma}, T, P) &= \frac{\eta_0(T, P)}{1 + (\eta_0 \dot{\gamma} / \tau^*)^{1-n}}, \\ \eta_0(T, P) &= D_1 \exp\left(\frac{-A_1(T - T_c)}{A_2 + (T - T_c)}\right), \\ T_c &= D_2 + D_3 P, \\ A_2 &= \tilde{A}_2 + D_3 \cdot P, \end{aligned} \quad (2)$$

where  $\eta$  is the viscosity of the melt,  $\eta_0$  is the zero shear viscosity,  $\dot{\gamma}$  is the shear rate,  $\tau^*$  is the material constant,  $n$  is the power law index in the shear rate,  $T$  is the melt temperature,  $T_c$  is the glass transition temperature, and  $D_1$ ,  $D_2$ ,  $D_3$ ,  $A_1$ , and  $\tilde{A}_2$  are the constants associated with the selected material.

**2.3. Fiber Orientation Model.** The fiber orientation is often described by two methods including orientation probability density distribution function and orientation tensor. The orientation probability density distribution function is used to calculate the ratio of short fibers to the total number of fibers in a certain orientation direction. It is intuitive and easy to understand, but its wide application is limited due to the large amount of calculation. In this work, the numerical simulation of SFO in WAIM is based on the fiber orientation tensor evolution equation. To succinctly represent the orientation of a large number of fibers, a second-order orientation tensor is defined as follows [18]:

$$\mathbf{A} = \oint \psi(\mathbf{P})\mathbf{P}\mathbf{P} d\mathbf{P} = \begin{bmatrix} A_{11} & A_{12} & A_{13} \\ A_{12} & A_{22} & A_{23} \\ A_{13} & A_{23} & A_{33} \end{bmatrix}, \quad (3)$$

$$A_{11} + A_{22} + A_{33} = 1,$$

where  $\psi(\mathbf{P})$  is the probability density distribution function of the whole orientation space,  $\mathbf{P}$  is the fiber's unit vector,  $\mathbf{A}$  is a symmetric matrix, and when  $\mathbf{A} = \mathbf{I}/3$ , it represents the orientation state isotropic, where  $\mathbf{I}$  represents an identity matrix. The three components  $A_{11}$ ,  $A_{22}$ , and  $A_{33}$  on the diagonal represent the fiber orientation in the melt flow direction, the cross-flow direction, and the thickness direction, respectively.

Tseng recently proposed a new fiber orientation prediction model (iARD-RPR) [21] as below:

$$\dot{\mathbf{A}} = \dot{\mathbf{A}}^{\text{HD}} + \dot{\mathbf{A}}^{\text{iARD}}(C_1, C_M) + \dot{\mathbf{A}}^{\text{RPR}}(\alpha), \quad (4)$$

where  $\dot{\mathbf{A}}^{\text{HD}}$  is a Jeffery hydrodynamic model,  $\dot{\mathbf{A}}^{\text{iARD}}$  is an improved anisotropic rotational diffusion model with two effective parameters: fiber-fiber interaction factor  $C_1$  ( $0 < C_1 < 0.1$ ) and fiber-matrix interaction influence factor  $C_M$  ( $0 < C_M < 1$ ), and  $\dot{\mathbf{A}}^{\text{RPR}}$  is the retarding principal rate model that contains the parameter  $\alpha$  ( $0 < \alpha < 1$ ), which is mean to slow the response rate of fiber orientation. The orientation tensor will be influenced by the parameters, and the default parameters ( $C_1 = 0.005$ ,  $C_M = 0.1$ , and  $\alpha = 0.7$ ) of iARD-RPR model for short fibers were used in the simulations:

$$\dot{\mathbf{A}}^{\text{HD}} = (\mathbf{W} \cdot \mathbf{A}) - (\mathbf{A} \cdot \mathbf{W}) + \xi(\mathbf{D} \cdot \mathbf{A} + \mathbf{A} \cdot \mathbf{D} - 2\mathbf{A}_4 : \mathbf{D}), \quad (5)$$

where  $\mathbf{W}$  is the vortex tensor,  $\mathbf{D}$  is the deformation rate tensor,  $\xi$  is the particle shape factor, and the fourth-order orientation tensor  $\mathbf{A}_4$  can be estimated from  $\mathbf{A}$  by using the eigenvalue-based optimal fitting (EBOF) closure [22] or the invariant-based optimal fitting (IBOF) closure [23]. EBOF was chosen in this paper.

$$\dot{\mathbf{A}}^{\text{iARD}} = \dot{\gamma}[2\mathbf{D}_r - 2\text{tr}(\mathbf{D}_r)\mathbf{A} - 5\mathbf{D}_r \cdot \mathbf{A} - 5\mathbf{A} \cdot \mathbf{D}_r + 10\mathbf{A}_4 : \mathbf{D}_r],$$

$$\mathbf{D}_r = C_1 \left( \mathbf{I} - C_M \frac{\mathbf{D}^2}{\|\mathbf{D}\|^2} \right),$$

$$\dot{\mathbf{A}}^{\text{RPR}} = -\mathbf{R} \cdot \dot{\mathbf{A}}^{\text{IOK}} \cdot \mathbf{R}^T,$$

$$\dot{\Lambda}_{ii}^{\text{IOK}} = \alpha \lambda_i, \quad i, j, k = 1, 2, 3, \quad (6)$$

where  $\dot{\mathbf{A}}^{\text{IOK}}$  is a material derivative of a diagonal tensor and its superscript is the intrinsic orientation kinetic (IOK) assumption,  $\dot{\Lambda}_{ii}^{\text{IOK}}$  is the  $i$ -th diagonal component of  $\dot{\mathbf{A}}^{\text{IOK}}$ ,  $\mathbf{R}$  is a rotation matrix,  $\lambda_i$  is the eigenvalue of matrix  $\mathbf{A}$ , and  $\lambda_1 > \lambda_2 > \lambda_3$ .

In the simulation, the melt flow problem was solved firstly, and then the resulting velocity field was applied to compute the short fiber orientation.

**2.4. Geometric Model.** The geometric model is shown in Figure 1. The length of the functional hollow duct is 245 mm, and the diameter is 20 mm. The overflow cavity was used to accommodate the melt pushed out by the high-pressure water. The connecting pipe between the duct and the overflow cavity had a diameter of 10 mm. The 3D model was created using Pro/E software. Moldex3D, developed by CoreTech System Co. Ltd., was used to simulate the melt filling and high-pressure water penetration process of WAIM. The combined model, imported into the Moldex3D R15.0, was meshed with Boundary Layer Mesh format. In the simulation, a short-fiber-reinforced PP (Fiberfil J-68/30/E with a short grass fiber mass fraction of 30% and an aspect ratio of 20) was selected as material, and its properties were available in the data bank of Moldex3D. The simulation of overflow WAIM process was carried out. First, the melt was injected into the mold cavity of the functional plastic part. Second, after a short delay time, the high-pressure water was injected into the core of the melt and penetrated along the core position with the least flow resistance and pushed the core melt into the overflow cavity to form a plastic part with a hollow cross section.

**2.5. Orthogonal Experimental Design.** During the injection molding process, due to the differences in viscosity gradient and velocity field distribution, the melt was sheared and stretched by the surrounding fluid, the shearing action causes the short fibers to align along the melt flow direction, and the stretching action causes the short fibers to orient along the stretch direction. Many factors affect the melt flow field in WAIM. The process parameters considered in this study include filling time ( $A$ ), melt temperature ( $B$ ), mold temperature ( $C$ ), delay time ( $D$ ), water pressure ( $E$ ), and water temperature ( $F$ ). These factors and their corresponding levels are listed in Table 1.

The full factorial experimental design method demands  $5^6$  experiments for 6 factors ( $A$ ,  $B$ ,  $C$ ,  $D$ ,  $E$ , and  $F$ ) with 5 levels. To reduce the number of experiments and comprehensively examine the influence of process parameters on SFO, the orthogonal experimental design ( $L_{25}(5^6)$ ) was used to arrange the test plan. In the final stage, the short fibers were mainly oriented along the melt flow direction. The values of the component of orientation tensor representing the melt flow direction were got at twenty different points along the thickness direction at the position I of RWT, and objective  $A_{11}$  is the average value of these points (Table 2).

**2.6. Range Analysis.** Range analysis, a statistical method, was used to analyze the experimental results obtained in the orthogonal experimental design. Range is defined as the difference between the maximum value and the minimum value. The factor with the maximum range is regarded as the most sensitive process parameter.

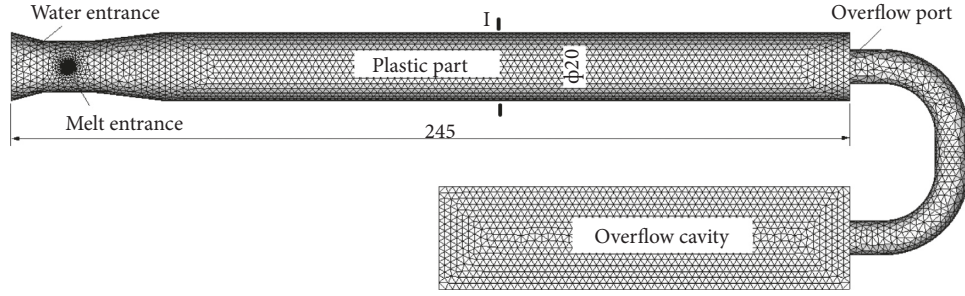


FIGURE 1: Geometric model for the numerical simulation experiment.

TABLE 1: Process parameters and levels of orthogonal experiment design.

Process parameters	Levels				
	1	2	3	4	5
Filling time (A) (s)	1	1.4	1.8	2.2	2.6
Melt temperature (B) (°C)	220	230	240	250	260
Mold temperature (C) (°C)	40	50	60	70	80
Delay time (D) (s)	1	1.5	2	2.5	3
Water pressure (E) (MPa)	6	6.5	7	7.5	8
Water temperature (F) (°C)	20	25	30	35	40

TABLE 2: Orthogonal experimental arrangement and results of simulation.

No.	A	B	C	D	E	F	A <sub>11</sub>
1	1	1	1	1	1	1	0.608
2	1	2	2	2	2	2	0.594
3	1	3	3	3	3	3	0.553
4	1	4	4	4	4	4	0.553
5	1	5	5	5	5	5	0.559
6	2	1	2	3	4	5	0.588
7	2	2	3	4	5	1	0.557
8	2	3	4	5	1	2	0.585
9	2	4	5	1	2	3	0.556
10	2	5	1	2	3	4	0.562
11	3	1	3	5	2	4	0.64
12	3	2	4	1	3	5	0.584
13	3	3	5	2	4	1	0.556
14	3	4	1	3	5	2	0.54
15	3	5	2	4	1	3	0.576
16	4	1	4	2	5	3	0.549
17	4	2	5	3	1	4	0.639
18	4	3	1	4	2	5	0.63
19	4	4	2	5	3	1	0.549
20	4	5	3	1	4	2	0.537
21	5	1	5	4	3	2	0.585
22	5	2	1	5	4	3	0.569
23	5	3	2	1	5	4	0.555
24	5	4	3	2	1	5	0.573
25	5	5	4	3	2	1	0.545

$$K_{ij} = \sum_{k=1}^{p_1} y_{ijk},$$

$$R_j = \max(K_{1j}, K_{2j}, \dots, K_{5j}) - \min(K_{1j}, K_{2j}, \dots, K_{5j}), \quad (7)$$

where  $i$  ( $i = 1, 2, 3, 4, 5$ ) is the level of a factor,  $j$  ( $j = A, B, C, D, E, \text{ and } F$ ) is a certain factor,  $K_{ij}$  is the sum value of  $A_{11}$  of all level in each factor,  $y_{ijk}$  is the value of the  $k$ -th experimental result,  $p_1$  is the test times with the  $j$ -th factor and the  $i$ -th level, and range  $R_j$  represents the influence degree of the factor. The larger the range  $R_j$  is, the stronger the influence of the factor is.

**2.7. Analysis of Variance.** Analysis of variance was employed to determine which factors were significant. In this method, the  $F$  value of each factor is used to indicate the degree of influence.

$$T = \sum_{i=1}^n \sum_{k=1}^{p_1} y_{ijk},$$

$$S_{\text{sum}} = \sum_{i=1}^n \sum_{k=1}^p (y_{ijk})^2 - \frac{T^2}{p_0},$$

$$S_j = \frac{\sum_{i=1}^n (K_{ij})^2}{p_1} - \frac{T^2}{p_0}, \quad (8)$$

$$S_e = S_{\text{sum}} - \sum_{j=1}^m S_j,$$

$$F = \frac{S_j/f_j}{S_e/f_e},$$

where  $T$  is the sum of test indexes,  $n$  is the number of levels,  $m$  is the number of factors,  $S_{\text{sum}}$  is the total differences,  $S_j$  is the differences of test results caused by the change in every level of factor  $j$ ,  $S_e$  is the differences of the test caused by the error,  $p_0$  is the total test times,  $f_j$  and  $f_e$  are the degrees of

freedom of each factor and test error, respectively, and other symbols are the same as above.

Given a significant level  $\alpha$ , the criterion  $F_\alpha(f_j, f_e)$  can be found in the  $F$  distribution table. The influence of a factor with  $F$  value greater than  $F_\alpha$  value is significant.

**2.8. Artificial Neural Network (ANN).** ANN inspired by the biologic neural system is a computing model used to map linear or nonlinear relationships between factors and responses. ANN can work as a human brain to establish a sample model from the perspective of information processing, without prior information or heuristic assumptions. An ANN model comprises three parts: one input layer, one or more hidden layers, and one output layer. The numbers of neurons in the input and output layer are determined by the numbers of factors and responses, respectively. In general, the number of neurons in hidden layer is determined by trial and error.

According to Kolmogorov's theorem [24], an ANN model with a single hidden layer has the ability to map any complex nonlinear relationship between input and output. In this study, an ANN model with one hidden layer was used for modeling. Gradient descent algorithm was used for training model. The transfer functions of *Tansig* and *Purelin* were employed in the hidden and output layer, respectively. By changing the number of neurons in the hidden layer from 5 to 15, the ANN topology of 6-13-1 with the minimum mean square error between the targets and the outputs was determined, indicating that there were six neurons in the input layer, thirteen neurons in the hidden layer, and one neuron in the output layer (Figure 2).

### 3. Results and Discussion

**3.1. Comparison between Simulation Result and Experimental Observation.** Figure 3 shows the component of orientation tensor along the melt flow direction in a section taken from the position I (Figure 1) of the model used in the simulation with each process parameter set to level 3. The values of  $A_{11}$  first increase and then decrease from the region near the mold cavity to the region near the water channel, and the larger values of  $A_{11}$  indicate more short fibers orient in the flow direction in the corresponding region. Based on the SFO in the flow direction, the RWT can be divided into two regions, such as the ordered region with large  $A_{11}$  and disordered region with small  $A_{11}$ . To verify the simulation results, water-assisted injection molded tubes with short-fiber-reinforced composite were observed by scanning electron microscopy (Nova NanoSEM 450) with an accelerating voltage of 5 kV. The tubes were produced by a laboratory-developed WAIM device improved from a 110-ton traditional injection molding machine. The material was PP containing 30% short grass fibers. The process parameters were set to the same as the simulation. A small sample was taken from the tube and immersed in liquid nitrogen for two hours and then cryofractured along the melt flow direction. The surface of the sample was subjected to gold-sputtered treatment before observation. Figure 4 shows that

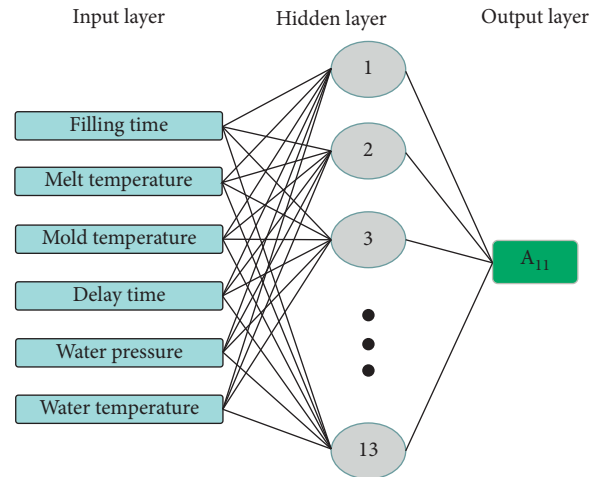


FIGURE 2: Topology of error back-propagation ANN.

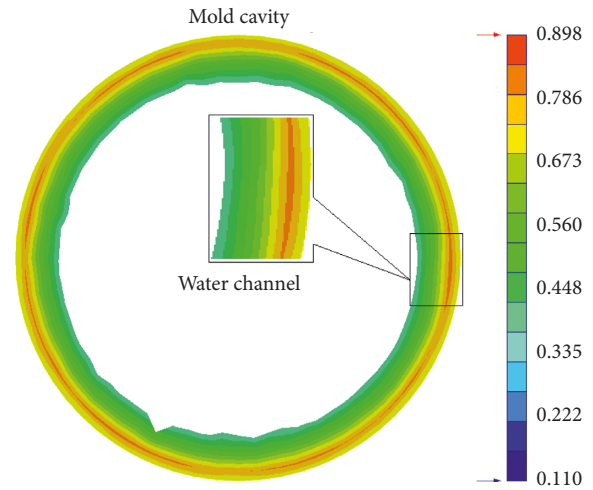


FIGURE 3: Contour of  $A_{11}$  in the RWT cross section.

the short fibers in the RWT mostly orient along the melt flow direction. Figures 4(a) and 4(b), the magnified micrographs taken from the ordered region and disordered region, indicate that more short fibers orient along the melt flow direction in the region near the mold cavity than that near the water channel. The experimental observations are consistent with the simulation results, indicating that the iARD-RPR model can well predict the SFO distribution in overflow WAIM.

#### 3.2. Analysis of Short Fiber Orientation Mechanism in WAIM.

Figure 5 shows the values of  $A_{11}$  obtained from 100 points along the diameter in the simulation. The melt filling process was similar to the conventional injection molding process, in which the short fibers oriented with a typical shell-core structure. The short fibers in the shell layer mainly oriented along the melt flow direction due to the shear action, whereas the short fibers in the core layer weakly oriented due to stretch action. The values of  $A_{11}$  increased from about 0.7 to 0.88 within the thickness of 0 to 2 mm. This could be

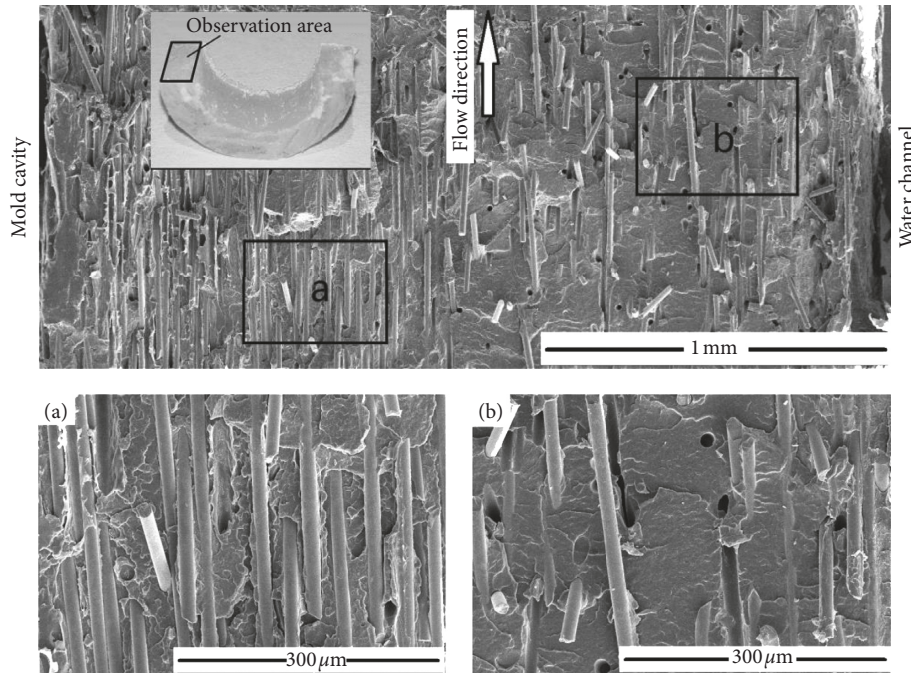


FIGURE 4: SEM micrographs of RWT: (a) ordered region and (b) disordered region.

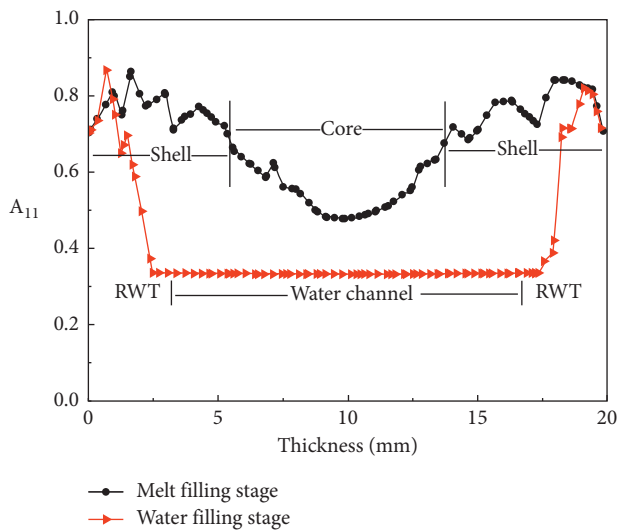


FIGURE 5: Distribution of SFO along the melt direction.

explained that the surface melt temperature decreases rapidly due to the cold mold cavity, and the short fibers are solidified without being sufficiently oriented; as the thickness increases, the cooling effect decreases and  $A_{11}$  increases.

In the water filling stage, the values of  $A_{11}$  in the region near the mold cavity are similar to that in the melt filling stage, which are caused by high shear action; the values of  $A_{11}$  decrease rapidly in the region near the water channel, indicating that the high-pressure water filling has an important influence on the SFO in this region. To prevent the occurrence of water vaporization, the water filling process lasts very short, and the water column in a turbulent state exerts strong squeezing and friction at the interface between

the melt and water. Furthermore, as the melt moves into the overflow cavity, the moving melt stretches the adjacent melt. The short fibers originally aligned along the flow direction readjust the posture due to the multiple disturbances, making short fibers in a disordered state in the region near water channel. In addition, the components of orientation tensors in all directions were assigned the values of 0.33 in the water channel with no fiber as shown in Figure 5.

**3.3. Sensitivity Analysis.** The results of range analysis are shown in Table 3. The rank of sensitivity of  $A_{11}$  to the six selected process parameters was determined and shown in the following based on the magnitude of the range  $R$  (water pressure, melt temperature, water temperature, mold temperature, filling rate, and delay time). As shown in Table 4, the results of the variance analysis indicate that the melt temperature and water pressure are highly significant factors for  $A_{11}$  with an  $F$  value of 7.346 and 8.612, respectively, and the water temperature with an  $F$  value of 4.102 is a significant factor for  $A_{11}$ . The filling rate, mold temperature, and delay time are not significant for  $A_{11}$  with the  $F$  values of 0.924, 1.163, and 0.913, respectively.

**3.4. Artificial Neural Network Modeling.** Experimental data (Table 2), obtained from orthogonal experimental design, were divided randomly into three data sets. 19 of overall 25 points were used to train the ANN model, and the others (3 + 3) were used to validate and test the model, respectively. The trained neural network was used to predict  $A_{11}$  in the orthogonal experimental scheme. As shown in Figure 6, the training sets and validation sets were almost on the diagonal line, and the test sets were very close to this line, indicating that the neural network has established the nonlinear

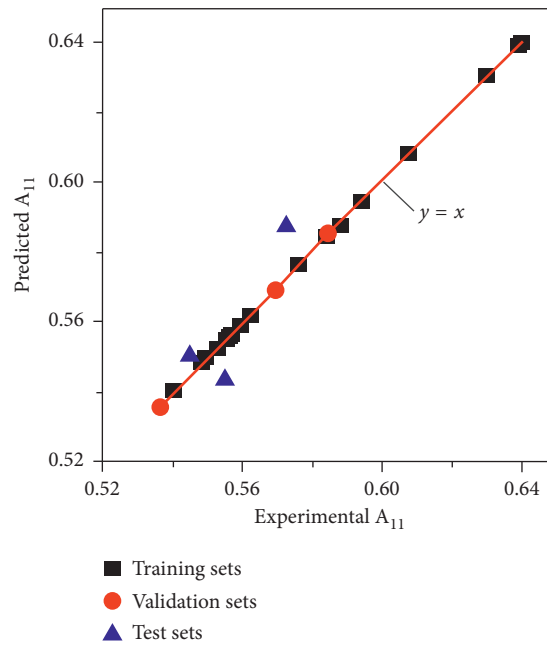
TABLE 3: Results of range analysis.

Factors	A	B	C	D	E	F
$K_{1j}$	2.8667	2.97	2.9105	2.8399	2.9812	2.8139
$K_{2j}$	2.8475	2.944	2.8624	2.8345	2.9657	2.8405
$K_{3j}$	2.8967	2.8784	2.8583	2.8649	2.8322	2.8042
$K_{4j}$	2.9043	2.7707	2.8163	2.9005	2.8025	2.949
$K_{5j}$	2.8272	2.7794	2.8949	2.9026	2.7609	2.9347
R	0.0772	0.1993	0.0942	0.0681	0.2203	0.1448
Rank	$E > B > F > C > A > D$					

TABLE 4: Results of variance analysis.

Factors	Sum of squares	Degree of freedom	Mean square	F value	$F_a$	Significant
A	$0.845E-3$	4	$0.211E-3$	0.924	$F_{0.05}(4, 12) = 3.26$	***
B	$0.672E-2$	4	$0.168E-2$	7.346		
C	$0.106E-2$	4	$0.266E-3$	1.163		
D	$0.834E-3$	4	$0.208E-3$	0.913	$F_{0.01}(4, 12) = 5.41$	***
E	$0.787E-2$	4	$0.197E-2$	8.612		
F	$0.375E-2$	4	$0.938E-3$	4.102		
Err.	$0.274E-2$	12	$0.228E-3$			**
Sum	0.0211	24				

\*\*Significant. \*\*\*Highly significant.

FIGURE 6: Predicted  $A_{11}$  values versus experimental  $A_{11}$  values.

relationship between the process parameters and  $A_{11}$  and could provide acceptable predictions.

**3.5. Interaction Effect of Significant Process Parameter.** Range and variance analysis results show that melt temperature, water pressure, and water temperature are significant for  $A_{11}$  of RWT in WAIM. The values of  $A_{11}$  were predicted by the trained neural network by changing two process parameters, while keeping the others constant. The 3D response surfaces and contour plots were used to describe the interaction effect of process parameters on  $A_{11}$ .

As shown in Figures 7 and 8, the value of  $A_{11}$  decreases as the melt temperature rises. The reasons come from two aspects. Firstly, the increasing melt temperature results in a decrease in viscosity. At the same shear rate, the shear stress decreases, and this is not conducive to the fiber orientation. Secondly, during the melt filling stage, the polymer molecular chains are also aligned, and the high melt temperature facilitates the deorientation behavior of the molecular chains after the completion of water injection process, which changes the orientation distribution of the short fibers and decreases  $A_{11}$ .

The values of  $A_{11}$  decrease with the increase in the water pressure (Figures 7 and 9). After melt filling stage, the short

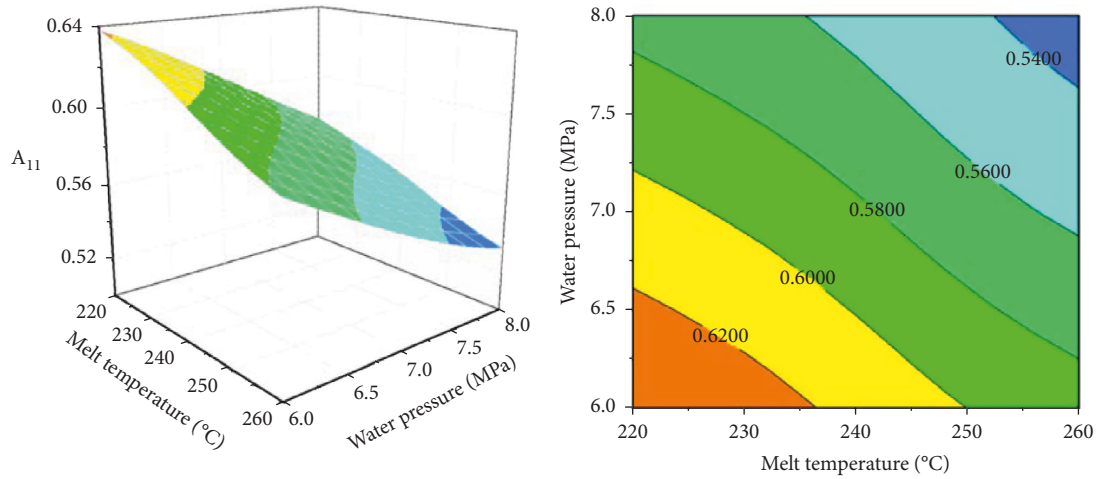


FIGURE 7: 3D response surface and contour plot of interaction effect of melt temperature and water pressure on  $A_{11}$ .

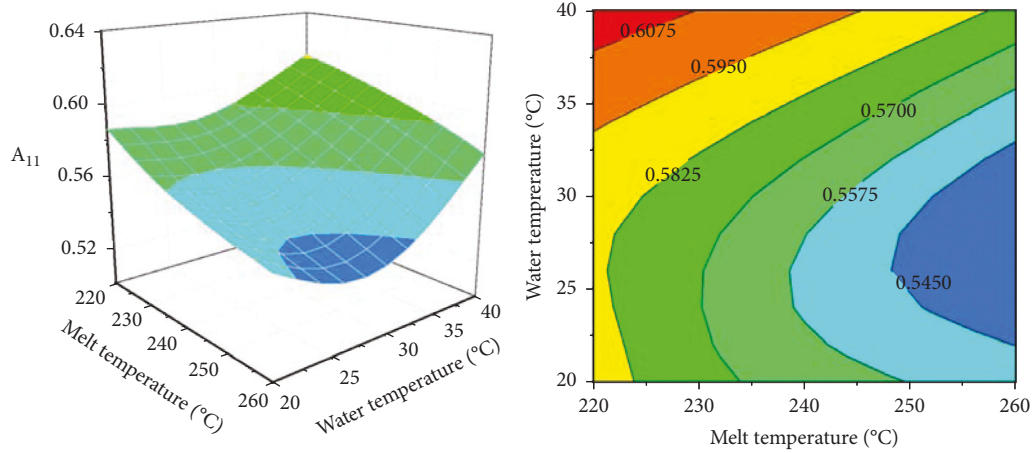


FIGURE 8: 3D response surface and contour plot of interaction effect of melt temperature and water temperature on  $A_{11}$ .

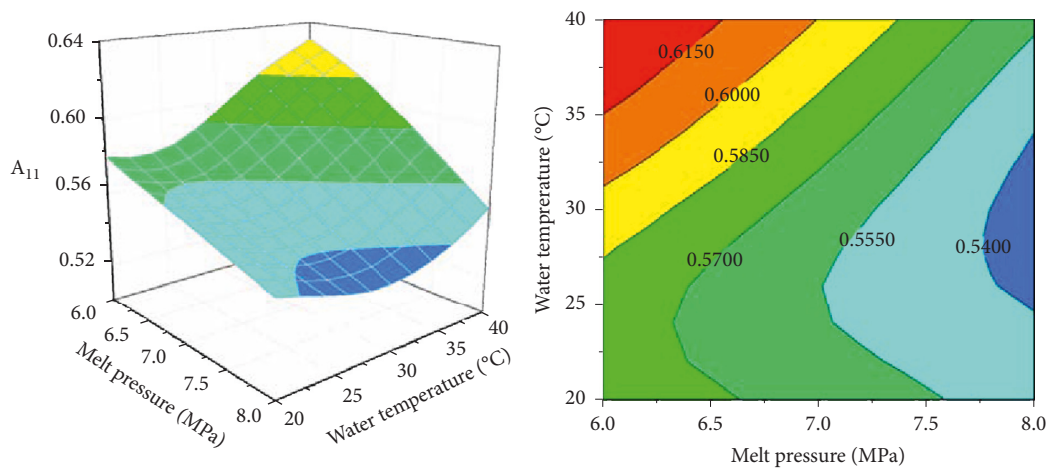


FIGURE 9: 3D response surface and contour plot of interaction effect of water pressure and water temperature on  $A_{11}$ .

fibers in the shell layer highly orient along the melt flow direction. During the high-pressure water filling stage, the inner layers of RWT bear the pressing and friction of water column as well as the stretching of the moving melt. The

short fibers originally oriented along the melt flow direction are posture-adjusted and arranged in a disordered state. The greater the water pressure is, the stronger the disturbance to the RWT is, and the smaller  $A_{11}$  in the melt flow direction is.

While the water injection temperature rises, the values of  $A_{11}$  of RWT in WAIM increase (Figures 8 and 9). The polymer melt has a viscoelastic property and can return to the original state after the external force is removed. The multiple disturbances cause the short fibers to be disordered in the inner layers of RWT during the water filling stage, and the higher water temperature favors the elastic recovery of the short fiber posture, thereby resulting in an increase of  $A_{11}$ .

#### 4. Conclusions

The iARD-RPR model was used to simulate the orientation of short fibers in WAIM. Compared with the SEM micrographs, the simulation results indicated that this model was suitable for the SFO prediction in overflow WAIM. The short fibers in the region near the mold cavity mostly oriented in the melt flow direction, while those in the region near the water channel were disordered. The melt temperature, water pressure, and water temperature have significant effects on the SFO along the melt flow direction. It was found that the values of  $A_{11}$  decreased with increasing water injection pressure and melt temperature and increased with increasing water temperature. Finally, this study is beneficial for the subsequent optimization of SFO in WAIM.

#### Data Availability

The data used to support the findings of this study are available from the corresponding author upon request.

#### Conflicts of Interest

The authors declare that there are no conflicts of interest regarding the publication of this paper.

#### Acknowledgments

This work was funded by the National Natural Science Foundation of China (Grant nos. 21664002 and 51563010) and the Jiangxi Provincial Key Technology R&D Program (Grant no. 20161BBE50073).

#### References

- [1] S. Mortazavian and A. Fatemi, "Fatigue behavior and modeling of short fiber reinforced polymer composites: a literature review," *International Journal of Fatigue*, vol. 70, pp. 297–321, 2015.
- [2] C. Röhrig, T. Scheffer, and S. Diebels, "Mechanical characterization of a short fiber-reinforced polymer at room temperature: experimental setups evaluated by an optical measurement system," *Continuum Mechanics and Thermodynamics*, vol. 29, no. 5, pp. 1093–1111, 2017.
- [3] B. M. Rudresh and B. N. Ravi Kumar, "Influence of experimental parameters on friction and wear mechanisms of PA66/PTFE blend reinforced with glass fiber," *Transactions of the Indian Institute of Metals*, vol. 71, no. 2, pp. 339–349, 2018.
- [4] S.-J. Liu and Y.-C. Wu, "Dynamic visualization of cavity-filling process in fluid-assisted injection molding-gas versus water," *Polymer Testing*, vol. 26, no. 2, pp. 232–242, 2007.
- [5] L. Li, Y. Peng, and W. Wei, "Recent advances on fluid assisted injection molding technique," *Recent Patents on Mechanical Engineering*, vol. 7, no. 1, pp. 82–91, 2014.
- [6] H. P. Park, B.-S. Cha, S.-B. Park et al., "A study on the void formation in residual wall thickness of fluid-assisted injection molding parts," *Advances in Materials Science and Engineering*, vol. 2014, Article ID 238251, 6 pages, 2014.
- [7] S. Liu, M. Lin, and Y. Wu, "An experimental study of the water-assisted injection molding of glass fiber filled polybutylene-terephthalate (PBT) composites," *Composites Science and Technology*, vol. 67, no. 7-8, pp. 1415–1424, 2007.
- [8] T. Q. Kuang, B. P. Xu, G. F. Zhou, and L. S. Turng, "Numerical simulation on residual thickness of pipes with curved sections in water-assisted co-injection molding," *Journal of Applied Polymer Science*, vol. 132, no. 34, pp. 1–10, 2015.
- [9] H. Park, B. S. Cha, and B. Rhee, "Experimental and numerical investigation of the effect of process conditions on residual wall thickness and cooling and surface characteristics of water-assisted injection molded hollow products," *Advances in Materials Science and Engineering*, vol. 2015, Article ID 161938, 11 pages, 2015.
- [10] J. G. Yang, X. H. Zhou, and Q. Niu, "Model and simulation of water penetration in water-assisted injection molding," *The International Journal of Advanced Manufacturing Technology*, vol. 67, no. 1–4, pp. 367–375, 2013.
- [11] T. Q. Kuang, K. Zhou, L. X. Wu, G. F. Zhou, and L. S. Turng, "Experimental study on the penetration interfaces of pipes with different cross-sections in overflow water-assisted coinjection molding," *Journal of Applied Polymer Science*, vol. 133, no. 1, pp. 1–8, 2016.
- [12] S.-J. Liu and Y.-S. Chen, "The manufacturing of thermoplastic composite parts by water-assisted injection-molding technology," *Composites Part A: Applied Science and Manufacturing*, vol. 35, no. 2, pp. 171–180, 2004.
- [13] S.-J. Liu and S.-P. Lin, "Study of "fingering" in water assisted injection molded composites," *Composites Part A: Applied Science and Manufacturing*, vol. 36, no. 11, pp. 1507–1517, 2005.
- [14] I. Fiebig and V. Schoeppner, "Factors influencing the fiber orientation in welding of fiber-reinforced thermoplastics," *Welding in the World*, vol. 62, no. 5, pp. 997–1012, 2018.
- [15] Q.-S. Jiang, H.-S. Liu, Q.-W. Xiao, S.-F. Chou, A.-H. Xiong, and H.-R. Nie, "Three-dimensional numerical simulation of total warpage deformation for short-glass-fiber-reinforced polypropylene composite injection-molded parts using coupled FEM," *Journal of Polymer Engineering*, vol. 38, no. 5, pp. 493–502, 2018.
- [16] S. C. Lee, D. Y. Yang, J. Ko, and J. R. Youn, "Effect of compressibility on flow field and fiber orientation during the filling stage of injection molding," *Journal of Materials Processing Technology*, vol. 70, no. 1-3, pp. 83–92, 1997.
- [17] H.-X. Huang, R.-H. Zhou, and C. Yang, "Fiber orientation propelled by high-pressure water penetration in water-assisted injection molded fiber-reinforced thermoplastics part," *Journal of Composite Materials*, vol. 47, no. 2, pp. 183–190, 2013.
- [18] S. G. Advani and C. L. Tucker, "The use of tensors to describe and predict fiber orientation in short fiber composites," *Journal of Rheology*, vol. 31, no. 8, pp. 751–784, 1987.
- [19] B. O. Agboola, D. A. Jack, and S. Montgomery-Smith, "Effectiveness of recent fiber-interaction diffusion models for orientation and the part stiffness predictions in injection molded short-fiber reinforced composites," *Composites Part A: Applied Science and Manufacturing*, vol. 43, no. 11, pp. 1959–1970, 2012.

- [20] H.-C. Tseng, R.-Y. Chang, and C.-H. Hsu, "Numerical prediction of fiber orientation and mechanical performance for short/long glass and carbon fiber-reinforced composites," *Composites Science and Technology*, vol. 144, pp. 51–56, 2017.
- [21] H.-C. Tseng, R.-Y. Chang, and C.-H. Hsu, "The use of shear-rate-dependent parameters to improve fiber orientation predictions for injection molded fiber composites," *Composites Part A: Applied Science and Manufacturing*, vol. 104, pp. 81–88, 2018.
- [22] J. S. Cintra Jr. and C. L. Tucker III, "Orthotropic closure approximations for flow-induced fiber orientation," *Journal of Rheology*, vol. 39, no. 6, pp. 1095–1122, 1995.
- [23] D. H. Chung and T. H. Kwon, "Invariant-based optimal fitting closure approximation for the numerical prediction of flow-induced fiber orientation," *Journal of Rheology*, vol. 46, no. 1, pp. 169–194, 2002.
- [24] V. Kůrková, "Kolmogorov's theorem and multilayer neural networks," *Neural Networks*, vol. 5, no. 3, pp. 501–506, 1992.



**Hindawi**  
Submit your manuscripts at  
[www.hindawi.com](http://www.hindawi.com)

